Eur. Phys. J. B **5**, 811–823 (1998)

THE EUROPEAN PHYSICAL JOURNAL B

Critical behavior of interacting surfaces with tension*

A. Volmer[1,a], U. Seifert[2], and R. Lipowsky[2]

[1] Institut für theoretische Physik, Universität Köln, Zülpicher Strasse 77, 50937 Köln, Germany
[2] Max-Planck-Institut für Kolloid- und Grenzflächenforschung, Kantstrasse 55, 14513 Teltow-Seehof, Germany

Received: 30 January 1998 / Accepted: 17 March 1998

Abstract. Wetting phenomena, molecular protrusions of lipid bilayers and membrane stacks under lateral tension provide physical examples for interacting surfaces with tension. Such surfaces are studied theoretically using functional renormalization and Monte-Carlo simulations. The critical behavior arising from thermally–excited shape fluctuations is determined both for global quantities such as the mean separation of these surfaces and for local quantities such as the probabilities for local contacts.

PACS. 64.60.-i General studies of phase transitions – 68.35.Ct Interface structure and roughness

1 Introduction

The surfaces considered here are interfaces and membranes which are governed by tension. An interface or domain wall which represents the stable contact region between two bulk phases of matter is always characterized by a finite interfacial tension, see, *e.g.*, [1]. Flexible membranes, on the other hand, are sheets of amphiphilic molecules such as lipid bilayers and are usually controlled by curvature and bending rigidity, see, *e.g.*, [2]. However, these membranes may be subject to an applied lateral tension arising from external forces or constraints. In addition, lipid bilayers exhibit molecular protrusions on small scales which are also governed by an effective tension.

In this paper, we study the interactions of two or several such surfaces and focus on the renormalization of these interactions arising from thermally–excited shape fluctuations. Physical examples are provided by (i) Wetting layers which are bounded by two interfaces; for reviews, see [3–6]. In this case, the interactions between these two interfaces are renormalized by capillary waves [7]; (ii) Lipid bilayers at separations which are small compared to the bilayer thickness. Such a situation arises for stacks of bilayers in the presence of a relatively large external pressure acting on these stacks. In this case, the interactions between adjacent bilayers are renormalized by molecular protrusions – thermally excited displacements of neighbouring lipid molecules which change the area of the lipid-water interface [8]; and (iii) Swollen bunches or stacks of membranes at separations which are large compared to the thickness of these membranes. This corresponds to the limit of relatively small external pressures acting on the membrane bunch or stack. Previous theoretical work on such bunches has focused on tensionless membranes as reviewed in reference [9]. In contrast, we will be concerned here with membranes under lateral tension.

The paper is organized as follows. In Section 2, we will define the theoretical models appropriate for (i) complete wetting, (ii) protrusion forces between bilayers, and (iii) membranes under lateral tension and explain that these models are equivalent to each other if the various parameters are identified in an appropriate way. In Section 3, we define the global and local critical effects which we will study in the remainder of the paper. One critical effect which has not been studied previously in a systematic way is the behavior of the probability for local contacts between the surfaces. Our results for two surfaces with hard wall and soft wall interactions are described in Sections 4 and 5, respectively.

In order to simplify the presentation, we will explicitly discuss our results in Sections 4 and 5 using the terminology of molecular protrusions for lipid bilayers. However, if one makes the appropriate identification of parameters as explained in Section 2, these results can be directly applied both to complete wetting and to membranes under lateral tension.

2 Theoretical framework

2.1 Wetting phenomena

Consider an interface between two bulk phases, say α and γ, and let us change a thermodynamic field, such as *e.g.* temperature or pressure, in order to move the system towards a triple point where a third phase, β, can coexist with the two phases α and γ. Then, in thermal equilibrium, a layer of the β phase may appear in the $\alpha\beta$ interface. As one comes closer and closer to the triple point,

* Dedicated to J. Zittartz on the occasion of his 60th birthday

[a] e-mail: av@thp.uni-koeln.de

the thickness of this intermediate layer may continuously grow: this is the case of *complete wetting*. On the other hand, no layer may appear in the $\alpha\beta$ interface or the thickness of this layer may saturate and remain finite as the triple point is attained: this is the case of *incomplete wetting*.

When the $(\alpha\gamma)$ interface contains a wetting layer of β phase, it splits up into an $(\alpha\beta)$ and a $(\beta\gamma)$ interface. The mean separation, $\ell \geq 0$, of these two interfaces is equal to the thickness of the wetting layer. Likewise, the excess free energy of the layer can be regarded as an effective interaction between these interfaces. Here, we will focus on the situation where the interaction potential between these two interfaces is purely repulsive and short–ranged. An example is provided by complete wetting in 3–dimensional lattice gas or Ising models.

2.1.1 Solid–on–solid models for wetting

Lattice gas or Ising models on a cubic lattice with a planar surface presumably provide the simplest models for wetting in three dimensions even though the corresponding phase diagram is already quite complex, see, *e.g.*, [10]. Wetting occurs at or close to two–phase coexistence provided the bulk of the system is in one phase, say in the spin–up phase (corresponding to the dilute vapor phase in the lattice gas) whereas the surface of the semi–infinite system favors the other phase (corresponding to the dense liquid phase in the lattice gas). In such a situation, one has a thin wetting layer of spin–down phase which is bounded (i) by the interface between this layer and the bulk phase and (ii) by the planar surface of the semi–infinite system.

At low temperatures, the interface is essentially flat. As one increases the temperature, typical excitations consist of islands on this flat interface. These excitations can be studied in the framework of so–called solid–on–solid models in which the planar surface of the semi–infinite system is described by a square lattice with lattice sites x_i and lattice constant a, and the local separation of the interface from this surface is described by the separation field $l_i \equiv l(x_i)$. The configurational energy or effective Hamiltonian of this separation field is given by

$$\mathcal{H}\{l\} = \sum_{\langle ij \rangle} (2J/a)|l_i - l_j| + \sum_i a^2 V(l_i) \qquad (2.1)$$

where $\langle ij \rangle$ indicates a summation over all nearest neighbors, J is the nearest neighbor coupling constant in the Ising model, and $V(l)$ denotes the effective potential acting on the interface [11]. For complete wetting, this potential has the simple form

$$V(l) = V_{hw}(l) + Hl \qquad (2.2)$$

where the hard–wall potential $V_{hw}(l)$ is defined by $V_{hw}(l) = 0$ for $l > 0$ and $V_{hw}(l) = \infty$ for $l < 0$ and H is the bulk magnetic field in the original Ising model. At temperature T (measured in energy units), the statistical weight for the configuration $l_i = l(x_i)$ is given by the Boltzmann factor $\sim \exp[-\mathcal{H}\{l\}/T]$.

2.1.2 Gaussian interface models for wetting

The model as given by (2.1) and (2.2) has been studied by Monte-Carlo simulations [12,13]. In these simulations, the mean separation of the two surfaces was determined in the limit of small magnetic field H. It was found that this quantity exhibits the same critical behavior in the discrete solid–on–solid model as in the corresponding Gaussian interface model. In its discrete version, the latter model is defined by the effective Hamiltonian

$$\mathcal{H}\{l\} = \sum_{\langle ij \rangle} \frac{1}{2} \Sigma (l_i - l_j)^2 + \sum_i a^2 V(l_i) \qquad (2.3)$$

where Σ represents the interfacial tension (or stiffness) of the fluctuating interface on large scales. In the continuum limit, this leads to

$$\mathcal{H}\{l\} = \int d^2x \left\{ \frac{1}{2} \Sigma (\nabla l)^2 + V(l) \right\} \qquad (2.4)$$

where both x and l are continuously varying coordinates. The latter model has been studied by functional renormalization as discussed in reference [8].

The critical behavior of the mean separation $\langle l \rangle$ is identical in the solid–on–solid and in the Gaussian model provided one identifies the interfacial tension with

$$\Sigma = c_\Sigma (2J/a)^2/T \qquad \text{with} \quad c_\Sigma \simeq 2.6 \qquad (2.5)$$

for the square lattice.

In the present work, we will address the question to what extent this correspondence between the two models is also valid for other quantities such as, *e.g.*, the probability for local contacts. In fact, we will see that the latter quantity has the same behavior for hard wall interactions but exhibits different behavior for soft wall interactions, see Section 5 below.

2.2 Molecular protrusions of bilayers

Now, let us consider a rather different system consisting of several lipid bilayers. It has been well–established by many experiments that such bilayers in aqueous solution experience strong repulsive forces at small separations of the order of 1 nm [14]. It was originally thought that this short–ranged repulsion represents a hydration effect and reflects the perturbed water structure in front of the polar head group [15]. More recently, it has been shown, however, that a similar repulsive force can also arise from the molecular roughness of the lipid–water interfaces.

Lipid bilayers consist of rod–like molecules with a hydrophilic head group and usually two hydrophobic tails. These rods are packed in such a way that the hydrophilic head groups shield the tails from the surrounding water. The corresponding lipid/water interface is roughened by thermally–excited fluctuations as has been observed in computer simulations [16,17] and has been deduced

from scattering experiments [18–20]. These thermal fluctuations correspond to protrusions, *i.e.*, to relative displacements or deformations of the lipid head groups. Since these protrusions will, in general, change the surface area of the lipid–water interface, they are governed by an effective tension.

The repulsive force arising from the protrusions of single molecules was calculated in reference [21]. The effect of collective protrusions which involve whole groups of lipid molecules was first studied in reference [8] within the framework of discrete and continuum interface models.

2.2.1 Models for collective protrusions

Consider one such lipid/water interface formed by the head groups of the lipid molecules which is located in front of a planar surface or wall. The head group at position x_i has the local separation l_i from the wall. If the lipid/water interface is flat, its separation from the wall is constant and all l_i are equal. Thermally–excited protrusions roughen this flat interface and lead to position–dependent configurations $l_i = l(x_i)$.

The configurational energy of these protrusions consists of two contributions. The first contribution is given by the excess free energy arising from the relative displacements of the molecules which is governed by the interfacial tension Σ_o. The latter quantity represents the free energy per unit area for the interface between the nonpolar part of the molecule and the water. In the discrete model to be defined, each molecule is supposed to have n_{nn} nearest neighbors. The molecular shape is approximated by a rigid column with circumference a_o and cross-sectional area A_o. For $n_{nn} = 6$, one has hexagonal columns on a triangular lattice with lattice constant $a = a_o/2\sqrt{3}$ and cross–sectional area $A_o = \sqrt{3}a^2/2$.

The second contribution to the configurational energy of the protrusions represents the excess free energy arising from the interaction of the lipid/water interface with the planar surface or wall. The corresponding interaction potential $V(l)$ has the generic form

$$V(l) = V_{hw}(l) + V_{hy}\exp[-l/l_{hy}] + Pl. \qquad (2.6)$$

The first term of $V(l)$ is again the hard wall repulsion which ensures that the two surfaces cannot penetrate each other. The second term in (2.6) represents the hydration interaction arising from the perturbed water structure in front of the lipid head groups; it is parameterized by a certain decay length l_{hy} and a certain amplitude V_{hy}. The last term Pl is the excess free energy arising from the external pressure P. For finite P, the lipid/water interface will have a finite mean distance from the wall and will undergo an unbinding transition in the limit of small P.

If one combines both contributions, one obtains the configurational energy or effective Hamiltonian [8]

$$\mathcal{H}\{l\} = \sum_{<ij>} (a_o\Sigma_o/n_{nn})|l_i - l_j| + \sum_i A_o V(l_i) \qquad (2.7)$$

for the collective protrusions described by the configuration $l_i = l(x_i)$. Comparison with the solid–on–solid model (2.1) shows that both models are completely equivalent.

The model as given by (2.7) was studied by Monte-Carlo simulations for a triangular lattice with $n_{nn} = 6$; in addition, the corresponding Gaussian model was studied by functional renormalization [8]. It was again found that the critical behavior of the mean separation is the same in both models provided one chooses the effective interfacial tension

$$\Sigma \equiv \Sigma_{pr} = c_\Sigma(a_o\Sigma_o/n_{nn})^2/T. \qquad (2.8)$$

For the triangular lattice with $n_{nn} = 6$ nearest neighbors, the Monte-Carlo simulations in references [8] lead to the estimate $c_\Sigma \simeq 2.4$ which is different from but close to the value $c_\Sigma \simeq 2.6$ as obtained for the square lattice.

2.3 Membranes under lateral tension

On sufficiently large scales, flexible membranes which do not experience any external force or constraint are governed by their bending rigidities and curvature energies, see the various reviews in reference [2]. On the other hand, the presence of such forces or constraints tends to induce lateral tensions which reduces the bending undulations of the membranes [22,23]. One example is provided by a closed vesicle which is inflated by an osmotic pressure difference $\Delta P = P_{in} - P_{ex}$. The surface of this vesicle will attain an essentially spherical shape with radius R_{ve} and the corresponding tension Σ satisfies the Laplace equation $\Sigma = R_{ve}\Delta P/2$.

If the vesicle is unilamellar, *i.e.*, if it is bounded by a single membrane, this membrane is subject to the tension Σ. If the vesicle is multi–lamellar, *i.e.*, if the vesicle surface consists of N closely packed membranes, each membrane should experience a lateral tension of the order of Σ/N.

It is also possible to apply a controlled suction pressure ΔP to the vesicle by micropipet aspiration [24,25]. In this way, one can directly control the lateral tension Σ. For a multi–lamellar vesicle, one then has N interacting membranes under lateral tension. In addition, the tense vesicle can also be pushed, via the micropipet, against a planar substrate or wall. Within the contact region, one then has an oriented stack interacting with the planar surface.

2.3.1 Continuum Gaussian models

Now, consider an oriented stack of membranes labeled by n with $1 \le n \le N$. Each membrane is characterized by its bending rigidity κ_n and is taken to experience the lateral tension Σ_n. For an oriented stack of membranes, the position of membrane n can be described by the height variables $h_n(x)$ which measures the distance from a reference plane with coordinate x. The interaction potential between two neighboring membranes is again denoted by $V(h_{n+1} - h_n)$. Using this parameterization, the effective

Hamiltonian for the whole stack has the form

$$\mathcal{H}\{h\} = \int d^2\mathbf{x} \left\{ \sum_{n=1}^{N} \left[\frac{1}{2}\Sigma_n \left(\nabla h_n\right)^2 + \frac{1}{2}\kappa_n \left(\nabla^2 h_n\right)^2 \right] + \sum_{n=1}^{N-1} V(h_{n+1} - h_n) \right\}. \tag{2.9}$$

For $N = 2$, one has a rigidity–dominated regime for sufficiently small scales and a tension–dominated regime for sufficiently large scales [2,26]. In the latter regime, the bending terms $\sim \left(\nabla^2 h_n\right)^2$ become irrelevant. Such a behavior is to be expected for general $N > 2$, and the critical behavior is then governed by the interplay between the tension terms and the interaction terms. In order to study this interplay, it is convenient to make an orthogonal transformation from rescaled height variables $\sqrt{\Sigma_n} h_n$ to new fields z_n which contain the 'center–of–mass' coordinate

$$z_N \equiv \sum_{n=1}^{N} \Sigma_n h_n \Big/ \left[\sum_{n=1}^{N} \Sigma_n \right]^{1/2}. \tag{2.10}$$

The latter coordinate decouples from the other fields z_n with $n < N$ since it does not enter in the interaction terms $\sim V(h_{n+1} - h_n)$. In this way, one arrives at models for the $N-1$ fields z_n with $n < N$ which are linear combinations of the $N-1$ separation fields $l_n \equiv h_{n+1} - h_n$. For $N = 2$, one obtains a model for the single field $z_1 \sim h_2 - h_1$ which is equivalent to the continuum Gaussian model for wetting as given by (2.4).

3 Critical behavior

In the following, we will discuss our results using the terminology which is appropriate for molecular protrusions of bilayers. The potentials $V(l)$ considered here consist of repulsive hard–wall and soft–wall interactions balanced by an external pressure term Pl as given in (2.6). In the present section, we will define the global and local quantities which become critical as the pressure P goes to zero.

3.1 Global quantities

Thus, consider two surfaces governed by tension which are pushed together by the external pressure P. The configuration of these two surfaces is described by their local separation $l = l(x)$. As P is decreased to zero, the two surfaces unbind which leads to the divergence of several length scales. First of all, the parallel correlation length $\xi_\parallel$ diverges as

$$\xi_\parallel \sim 1/P^{\nu_\parallel} \tag{3.1}$$

which defines the critical exponent $\nu_\parallel$.

In addition, both the mean separation $\ell \equiv \langle l \rangle$ of the two surfaces and the roughness

$$\xi_\perp \equiv \left\langle (l - \langle l \rangle)^2 \right\rangle^{1/2} \tag{3.2}$$

of the separation field l are singular for small P. For protrusions, which are governed by the effective tension $\Sigma = \Sigma_{pr}$ as in (2.8), the interfacial roughness is related to $\xi_\parallel$ *via*

$$\xi_\perp \approx (T/2\pi\Sigma)^{1/2} \sqrt{\ln(\xi_\parallel/a)} \tag{3.3}$$

where a denotes the small–scale cutoff as before [7]. This relation is analogous to the well–known scaling of the roughness of a free interface as a function of its linear dimension. Note that the basic length scale which sets the size of the interfacial roughness is given by the protrusion length

$$l_{pr} \equiv (T/2\pi\Sigma)^{1/2}. \tag{3.4}$$

For three surfaces, one has two separation fields $l_1 = h_2 - h_1$ and $l_2 = h_3 - h_2$. In this case, one convenient choice is to use the two fields $d_1 \sim l_1 + l_2$, which is the thickness of the whole bunch, and $d_2 \sim l_1 - l_2$.

3.2 Local contacts

As the surfaces unbind, the probabilities for local contacts of the surfaces decay to zero. More precisely, the probability $\mathcal{P}_{2b}$ for pair contacts is found to behave as

$$\mathcal{P}_{2b} \sim 1/\xi_\parallel^{\zeta_2} \sim P^{\nu_2} \tag{3.5}$$

which defines the critical exponents ν_2. This exponent satisfies the scaling relation

$$\nu_2 \equiv \zeta_2 \nu_\parallel. \tag{3.6}$$

For a bunch of three or more interacting surfaces, one may consider the probabilities $\mathcal{P}_{nb}$ for local n–contacts. These quantities have the scaling behavior

$$\mathcal{P}_{nb} \sim 1/\xi_\parallel^{\zeta_n} \sim P^{\nu_n} \qquad \text{with} \quad \nu_n \equiv \zeta_n \nu_\parallel. \tag{3.7}$$

Local contacts have also been studied for 1-dimensional lines (or strings or directed walks) governed by line tension [27–30] and for tensionless membranes [30]. In the following sections, we will study these quantities for two and three interacting surfaces governed by tension.

4 Two surfaces with hard wall interactions

In this section, we study the critical behavior of two surfaces interacting with hard wall interactions $V_{hw}(l)$ with $V_{hw}(l) = 0$ for $l > 0$ and $V_{hw}(l) = \infty$ for $l < 0$ as before. Since this interaction contains no length and no energy

scale, it does not introduce any dimensionfull parameter into the model.

We begin with a brief summary of the results from a functional renormalization group treatment, which gives predictions for the mean distance ℓ and the roughness $\xi_\perp$ of the interfaces. Additionally, we consider the pair contact probability $\mathcal{P}_{2b}$ and derive predictions for its scaling behavior. Monte-Carlo (MC) simulations are used to test the theoretical results. The Gaussian and the solid–on–solid model are treated separately.

4.1 Gaussian models

First, we give a short review of the functional renormalization group treatment of the Gaussian model as defined by (2.4), following [8]. The functional renormalization group is used to integrate out thermal fluctuations on scales between the microscopic length a and the lateral correlation length $\xi_\parallel$, which will be finite for finite values of the pressure P. Technically, this integration is performed in a one-step nonlinear functional renormalization group with a rescaling factor $b = \xi_\parallel/a$, using a formalism which is an extension of Wilson's approximate recursion relation [31], and which has been developed in studies of the wetting transition [7]. This procedure yields an effective interaction potential on the scale of the lateral and perpendicular correlation lengths $\xi_\parallel$ and $\xi_\perp$. Now, on this scale, mean field theory can be used, allowing to set up a self consistent procedure to determine the mean separation $\ell \equiv \langle l \rangle$, $\xi_\perp$ and $\xi_\parallel$ by minimizing the effective potential. This effective potential is now, on the scale $\xi_\parallel$, defined as a simple superposition of the effective hard wall potential and a linear pressure term:

$$V^{\mathit{eff}}(l) \equiv V_{hw}^{\mathit{eff}}(l) + Pl, \tag{4.1}$$

where $V_{hw}^{\mathit{eff}}(l) = -\tilde{v} \ln \mathrm{erf}(l/\sqrt{2}\xi_\perp)$. The parameter $\tilde{v} \simeq T/A_o$ represents the basic energy scale.

Minimization with respect to l leads to

$$P = -\left.\frac{\partial V_{hw}^{\mathit{eff}}}{\partial l}\right|_{l=\ell} \approx \frac{\sqrt{2}\tilde{v}}{\sqrt{\pi}\xi_\perp} e^{-\ell^2/2\xi_\perp^2}. \tag{4.2}$$

In addition, we have the mean field relation between $\xi_\parallel$ and the curvature of the effective potential in the minimum position

$$\frac{\Sigma}{\xi_\parallel^2} = \left.\frac{\partial^2 V_{hw}^{\mathit{eff}}}{\partial l^2}\right|_{l=\ell} \tag{4.3}$$

and the relation between the two length scales $\xi_\parallel$ and $\xi_\perp$ as given in (3.3). Solution of this set of equations yields a relation between the pressure and the mean separation ℓ that is given by

$$P \approx P_{hw} e^{-\ell/l_{pr}} (l_{pr}/\ell)^{1/4}, \tag{4.4}$$

with the protrusion length $l_{pr} = (T/2\pi\Sigma)^{1/2}$ as before. Likewise, the surface roughness $\xi_\perp$ is found to obey the relation

$$P \approx P_{hw\perp} e^{-2(\xi_\perp/l_{pr})^2}. \tag{4.5}$$

The two pressure amplitudes take the form

$$P_{hw} = \frac{\sqrt{\Sigma\tilde{v}}}{\pi^{1/4} a} \qquad \text{and} \qquad P_{hw\perp} = \frac{l_{pr}\Sigma}{2a^2}\,. \tag{4.6}$$

Inverting the two relations (4.4) and (4.5), one finds

$$\ell \approx l_{pr}\,[\,\ln(P_{hw}/P) - 1/4\ \ln\ln(P_{hw}/P)\,] \tag{4.7}$$

and

$$\xi_\perp^2 \approx l_{pr}^2/2\ \ln(P_{hw\perp}/P) \tag{4.8}$$

in the limit of small P.

The mean separation and the correlation lengths represent global quantities of the interface. In order to introduce a local quantity, namely the pair contact probability $\mathcal{P}_{2b}$, we define the probability distribution

$$\mathcal{P}_\Delta(l) \equiv \langle\, \theta(l + \Delta l) - \theta(l)\,\rangle/\Delta l, \tag{4.9}$$

where $\theta(l)$ is the Heaviside step function and Δl is a microscopic length scale. $\mathcal{P}_\Delta(l)$ gives the probability to find the surface height $l(x)$, at a given position x, in the interval $l \ldots l + \Delta l$. Then, the probability $\mathcal{P}_{2b}$ for pair contacts is given by

$$\mathcal{P}_{2b} = \mathcal{P}_\Delta(l = 0). \tag{4.10}$$

In the following, we will omit the subscript Δ, and take Δl to be a fixed microscopic length scale Δl. If one assumes that $\mathcal{P}(l)$ is well approximated by a Gaussian distribution which is centered at the mean separation ℓ and has the width $\simeq \xi_\perp$, the pair contact probability is given by

$$\mathcal{P}_{2b} \sim \exp[-\ell^2/2\xi_\perp^2]/\xi_\perp. \tag{4.11}$$

Note that in the Gaussian case, the full distribution $\mathcal{P}(l)$ is fully determined by its first two moments, ℓ and $\xi_\perp^2$. Inserting the asymptotic pressure dependence of these two length scales, as given by (4.7) and (4.8), into (4.11), one immediately obtains

$$\mathcal{P}_{2b} \sim \exp\left[-\ln^2(P_{hw}/P)\ /\ \ln(P_{hw\perp}/P)\right] \tag{4.12}$$

$$\sim P^{\nu_2} \qquad \text{with} \quad \nu_2 = 1, \tag{4.13}$$

neglecting confluent logarithmic corrections to the leading scaling behavior. The contact exponent ν_2, which has been introduced in Section 3.2, governs the asymptotic behavior for $P \gg P_{hw}$ and $P \gg P_{hw\perp}$.

The above assumption about the Gaussian character of the probability distribution $\mathcal{P}(l)$ has been confirmed by Monte-Carlo simulations of the discrete Gaussian model. In the simulations, the discrete form

$$\bar{\mathcal{H}}\{z\} \equiv \frac{\mathcal{H}\{z\}}{T} = \sum_{\langle i,j \rangle} \frac{(z_i - z_j)^2}{2n_{nn}} + \sum_i (U_{hw}(z_i) + Qz_i) \tag{4.14}$$

of the effective Hamiltonian has been studied, where we have used the dimensionless quantities $z \equiv l/l_{sc}$ and $Q \equiv P/P_{sc}$ with

$$l_{sc} = \sqrt{T/\Sigma n_{nn}} \qquad \text{and} \qquad P_{sc} = \sqrt{T\Sigma n_{nn}}/a^2. \quad (4.15)$$

For all MC simulations, a triangular lattice with 6 nearest neighbours per site was used, and the simulated area had the form of a parallelogram. Periodic boundary conditions were applied in the direction parallel to the base line of the parallelogram and in the direction perpendicular to this line. The linear dimensions in both directions were always taken to be equal. Typical lattice sizes were $L_\parallel$=32 and 64, where $L_\parallel$ is the linear dimension. For optimization of calculation time, the height variables z_i were discretized; we have checked, however, that the results do not differ from those obtained when using floating point variables. Finally, the acceptance rate of the MC step was continuously controlled by tuning the maximum height variation per step and site. The length of the MC runs varied between 10^5 and 10^6 MC steps per site, depending on the chosen value of the external pressure Q.

The statistical errors of the MC results were controlled in the following way. Starting with a small MC sampling interval Δt, the mean values of all observables were measured within n equal intervals of length $\Delta t/n$, giving n values A_μ with $\mu = 1, ..., n$. Usually, we have chosen the value $n = 10$. From these values, the statistical error δA, defined as $\delta A^2 = \langle\, [\, \frac{1}{n} \sum_{\mu=1}^{n} (A_\mu - \langle A \rangle)\,]^2 \,\rangle$, was calculated. Then, Δt was multiplied by n, and the procedure was repeated on the larger time scale. In this way, one can plot the relative statistical error $\delta A/\langle A \rangle$ of the observable A as a function of Δt. The results of this procedure are illustrated in Figure 1. Note that when Δt becomes larger than the relaxation time, the relative error decreases monotonically. In the MC results presented in this paper, we have plotted no error bars because the statistical errors were typically smaller than the data symbols.

MC data of probability distributions $\mathcal{P}(l)$ for three different values of the pressure Q are shown in Figure 2. These data were obtained in simulations of one flexible surface pushed against a hard wall, and are well fitted by Gaussian distributions.

Consequently, the value $\nu_2 = 1$ of the contact exponent is confirmed by MC simulations of the discrete Gaussian model. Similar data have been obtained in simulations of the solid–on–solid model as explained in the next section.

In addition, the predictions for the global quantities ℓ and $\xi_\perp$, as given by (4.7) and (4.8), have been confirmed in our simulations. The corresponding data are not shown here since they are similar to the corresponding data for the solid–on–solid model shown in the next section. From the fits of the mean distance ℓ to the functional form as given by (4.7), we have extracted the dimensionless protrusion length $z_{pr} \equiv l_{pr}/l_{sc} = 0.55 \pm 0.02$. We have checked that this value of z_{pr} is consistent with the fits of the roughness $\xi_\perp$ as in (4.8).

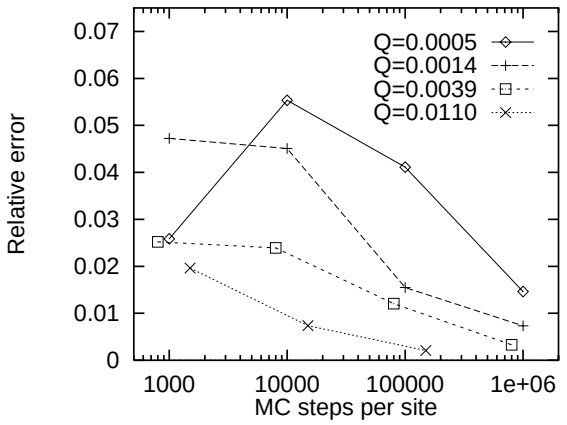

Fig. 1. Some typical values for the relative error of the measured mean distance as a function of the simulation time, measured in MC steps per site Δt. The SOS model with one flexible surface fluctuating against a hard wall was simulated, with a system of linear dimension $L_\parallel = 64$.

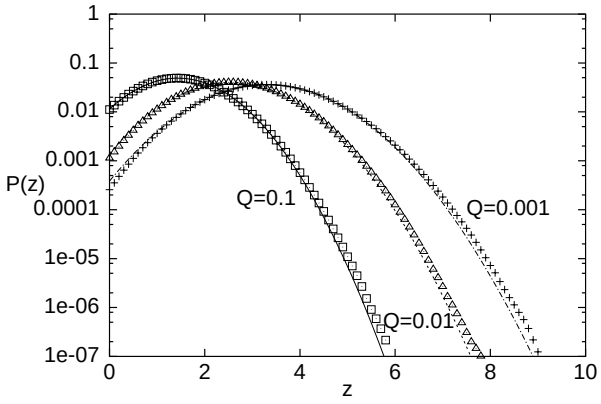

Fig. 2. Probability distribution $\mathcal{P}(z)$ for the discrete Gaussian model of a fluctuating surface which is pushed against a hard wall by the external pressure Q. The data points are fitted by Gaussians.

4.2 Solid–on–solid models

In order to set up Monte-Carlo simulations of the solid–on–solid model for collective protrusions as defined by (2.7), we use the dimensionless length $z \equiv l/l_{sc}$ and pressure $Q \equiv P/P_{sc}$, where the length and the pressure scale are now given by

$$l_{sc} = T/a_0\Sigma_0 \qquad \text{and} \qquad P_{sc} = a_0\Sigma_0/A_0. \qquad (4.16)$$

In terms of these rescaled quantities, the effective Hamiltonian for one protruding surface reads

$$\bar{\mathcal{H}}\{z\} = \sum_{\langle ij \rangle} |z_i - z_j|/n_{nn} + \sum_i (Qz_i + U_{hw}(z_i)), \quad (4.17)$$

where n_{nn} is the number of nearest neighbours of each molecule as before. The generalization for two protruding

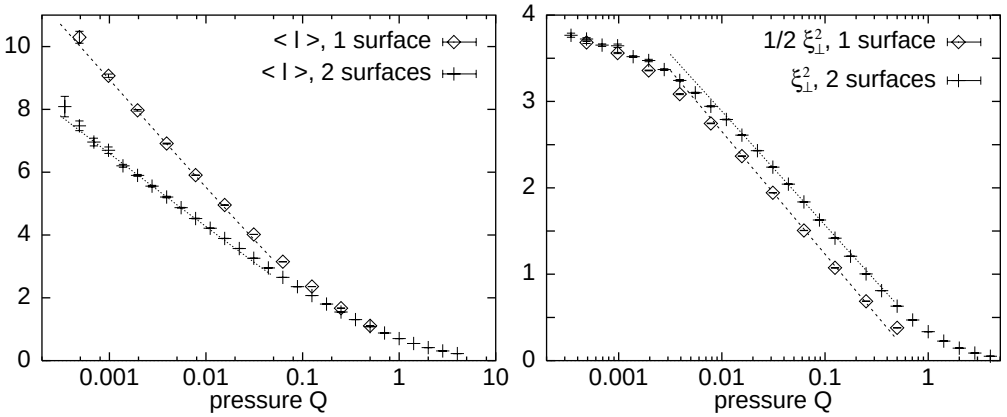

Fig. 3. MC data for the SOS model. Mean distance ℓ (*left*) and roughness $\xi_\perp^2$ (*right*) *versus* pressure Q, both in the case of one and of two fluctuating surfaces. The mean distance is fitted by $\ell \simeq l_{pr}(\ln(Q_{hw}/Q) - 1/4 \ln\ln(Q_{hw}/Q))$, see equation (4.7), with $l_{pr} = 1.57$ and $Q_{hw} = 0.47$ for one surface and $l_{pr} = 1.06$, $Q_{hw} = 0.81$ for two surfaces. The values for the roughness are fitted by $\xi_\perp^2 \simeq l_{pr}^2/2 \ln(Q_{hw\perp}/Q)$, see equation (4.8), with $Q_{hw\perp} = 0.74$ for one surface and $Q_{hw\perp} = 1.55$ for two surfaces.

surfaces is obvious and leads to

$$\bar{\mathcal{H}}\{z_1, z_2\} = \sum_{\langle ij \rangle} \frac{1}{n_{nn}} \left(|z_{1,i} - z_{1,j}| + |z_{2,i} - z_{2,j}|\right) + \sum_i Q\,(z_{1,i} - z_{2,i}) + U_{hw}(z_{1,i} - z_{2,i}), \quad (4.18)$$

which, after introducing the difference coordinate $z \equiv z_1 - z_2$ and the center–of–mass coordinate $\bar{z} \equiv z_1 + z_2$, takes the form

$$\bar{\mathcal{H}}\{\bar{z}, z\} = \sum_{\langle ij \rangle} \frac{1}{n_{nn}} \mathrm{Max}(|\bar{z}_i - \bar{z}_j|, |z_i - z_j|) + \sum_i Q\, z_i + U_{hw}(z_i). \quad (4.19)$$

Note that in the solid–on–solid (SOS) model, the center–of–mass coordinate and the difference coordinate do not decouple, in contrast to the Gaussian model. By this decoupling, the Gaussian model with two surfaces can be exactly mapped to a model for two independent surfaces, one of which is free (the center–of–mass coordinate), the other one being subject to the external potential (the difference coordinate). We have employed Monte-Carlo simulations in order to check whether the critical behavior of global quantities in the SOS model for two interfaces as given by (4.18), is nevertheless consistent with the behavior obtained from the Gaussian model.

This assumption is indeed confirmed by the results from MC simulations, as shown in Figure 3. There, the mean distance ℓ and the roughness $\xi_\perp$ are plotted *versus* the pressure Q, both in the case of one and of two fluctuating surfaces. The length scale $l_{pr(2)}$ in the latter case relates to the protrusion length l_{pr} as defined in (3.4) in the following way, using the terminology of the membrane model: Consider the surface tension Σ of a single membrane surface in the Gaussian model. First, in the case of two identical surfaces, the reduced surface tension Σ_r of the distance coordinate $l_1 - l_2$ is given by $\Sigma/2$. Second, the microscopic tension Σ_0 has to be multiplied by 2 since two adjacent molecules in the lipid bilayer should move coherently in order to prevent the generation of energetically unfavorable cavities between them. With $\Sigma \sim \Sigma_0^2$ as in (2.8), these two effects lead to $l_{pr(2)} = l_{pr}/\sqrt{2}$.

The actual values for z_{pr}, as extracted from the simulations results in the same way as described in the preceding chapter on the Gaussian model, are $z_{pr} = 1.57 \pm 0.03$ for one surface and $z_{pr(2)} \simeq 1.07 \pm 0.02$ for two surfaces. The corresponding fits are shown in Figure 3.

Let us shortly focus on the high pressure regime with $Q \gtrsim 1$. In this regime, the dimensionless external pressure Q is larger than the microscopic surface tension (which has been scaled to 1), so the molecules move almost independently. Hence neglecting the elastic term in the Hamiltonian, the partition sum in this regime is asymptotically given by

$$\Xi(Q) \approx \prod_{i=1}^{N} \int_0^\infty e^{-Qz_i} dz_i = \frac{1}{Q^N}, \quad (4.20)$$

which leads to the mean separation

$$\langle z \rangle = \frac{1}{N} \sum_i \langle z_i \rangle = -\frac{1}{N} \frac{\partial}{\partial Q} \ln \Xi(Q) = \frac{1}{Q}\,. \quad (4.21)$$

In the same way, one obtains the surface roughness $\xi_\perp \sim 1/Q$. These results are displayed in Figure 4.

Now, let us inspect the probability distribution $\mathcal{P}(l)$, as defined in (4.9), in the SOS model. Except for its tails far away from the hard wall, $\mathcal{P}(l)$ is rather well fitted by a Gaussian distribution of the form

$$\begin{aligned} \mathcal{P}_{\mathrm{fit}}(l) &= \frac{\alpha}{\sqrt{2\pi}\xi_\perp} \exp\left(-\frac{(l-\ell)^2}{2\xi_\perp^2}\right) \quad \text{for } l > 0 \\ &= \quad 0 \qquad\qquad\qquad\qquad\quad \text{for } l < 0. \end{aligned} \quad (4.22)$$

This is shown in Figure 5, where the rescaled functions $\xi_\perp \mathcal{P}((l - l_{max})/\xi_\perp)$ collapse almost onto a single

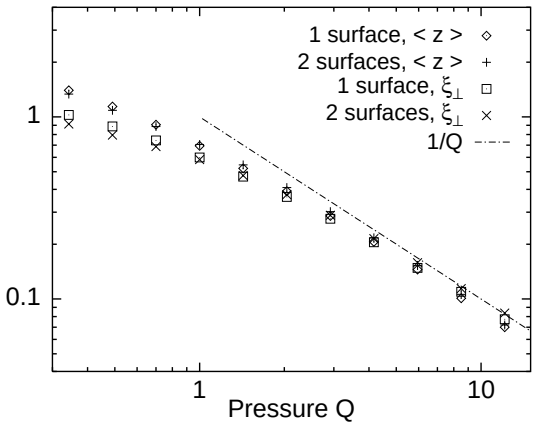

Fig. 4. Mean distance $\langle z \rangle$ and roughness $\xi_\perp$ *versus* pressure Q in the high pressure regime for the SOS-model. The MC data were obtained for a pure hard wall potential and a triangular lattice with linear dimension $L_\parallel = 32$.

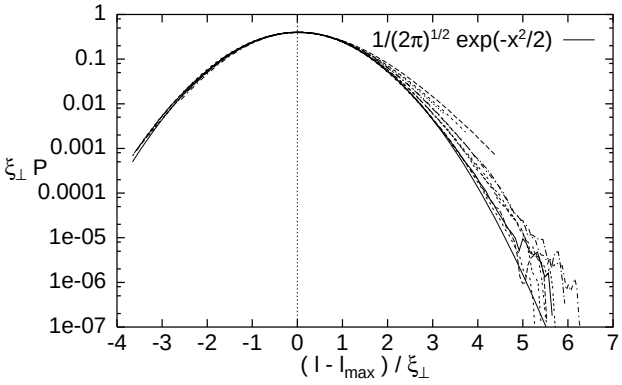

Fig. 5. Data collapse $\xi_\perp \mathcal{P}((l - l_{max})/\xi_\perp)$ for two surfaces in the SOS model, for 11 different values of the external pressure in the range $Q = 5 \times 10^{-5} - 7 \times 10^{-2}$. l_{max} is the most probable distance between the two surfaces. The topmost curve, which most strongly deviates from the Gaussian, corresponds to the highest pressure value.

curve which coincides well with the Gaussian distribution $\mathcal{P}_{\rm fit}(l)$. For distances $l \lesssim \ell$, *i.e.*, on the side facing the hard wall, $\mathcal{P}(l)$ does indeed not deviate substantially from the Gaussian. Hence, our argument leading to the prediction $\nu_2 = 1$ for the contact exponent as in (4.12) also applies to the SOS model. The scaling behavior for the probability for local pair contacts $\mathcal{P}_{2b}$ is fully confirmed by numerical results which have been obtained over a pressure range of five orders of magnitude, see Figure 6.

For $l > \ell$, on the other hand, substantial deviations from the Gaussian behavior are observed since the histograms have an exponential tail; see also Figure 7. This tail results from isolated protrusions, which can be understood as follows. The energy of an isolated protrusion of height l is given by $E(l) = \sum_{n.n.} |l_i - l|/(n_{nn} l_{sc})$, which, if all neighbouring sites i have heights $l_i < l$, simplifies to $E(l) = |\bar{l}_{nn} - l|/l_{sc}$, with $\bar{l}_{nn} = n_{nn}^{-1} \sum_{n.n.} l_i$. Together

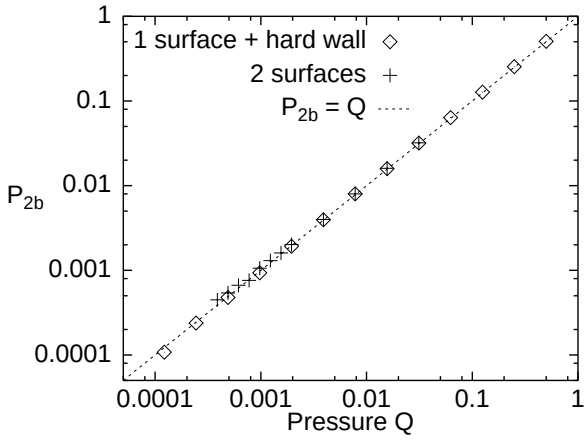

Fig. 6. Contact probability $\mathcal{P}_{2b}$ *versus* pressure Q for the SOS-model. The dotted line corresponds to the value $\nu_2 = 1$ for the contact exponent. It turns out that $\mathcal{P}_{2b} = \alpha Q$ with $\alpha \simeq 1$.

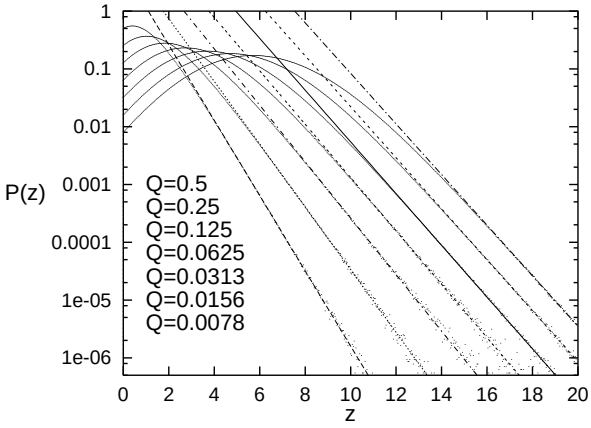

Fig. 7. Probability distribution $\mathcal{P}(z)$ for one fluctuating surface with hard wall interaction within the SOS model. The tails have been fitted by exponentials of the form $c\, e^{-z(1+Q)}$, where the amplitude c represents a fit parameter.

with the external pressure term Q, the probability of a single protrusion is hence proportional to $e^{-z(1+Q)}$. The fits in Figure 7 confirm this simple explanation.

5 Two surfaces with soft wall interactions

Now, we will study two surfaces which are governed by the potential

$$V(l) = V_{hw}(l) + V_{hy} \exp[-l/l_{hy}] + Pl \qquad (5.1)$$

which includes the hydration interaction $V_{hy} e^{-l/l_{hy}}$. The decay length of this soft wall is given by the hydration length l_{hy}, which introduces a new length scale into the problem.

Linear functional renormalization of the hydration interaction shows that the interplay between the protrusion length l_{pr} and the hydration length l_{hy} leads to two different regimes [8]: For $l_{pr} > 2\, l_{hy}$ and $l_{pr} < 2\, l_{hy}$, one has

a *protrusion regime* and a *hydration regime*, respectively. In the protrusion regime, the asymptotic behavior is the same as in the case of a hard–wall interaction alone. In the hydration regime, on the other hand, one finds qualitatively new behavior.

Within the hydration regime, the relation between the pressure P and the interfacial roughness $\xi_\perp$ has again the Gaussian form as given by (4.5) but with the new pressure amplitude $P_{2\perp} = l_{hy}\Sigma/a^2$. The relation between the pressure and the mean distance ℓ, on the other hand, is now given by

$$P \approx P_2\, e^{-\ell/l_t} \tag{5.2}$$

which is governed by the new length scale

$$l_t = l_{hy}\, \left[1 + (l_{pr}/2l_{hy})^2\right]. \tag{5.3}$$

The pressure amplitude P_2 has the parameter dependence

$$P_2 = (\Sigma/a^2)^\rho\, V_{hy}^{1-\rho}\, l_{hy}^{2\rho-1} \tag{5.4}$$

with $\rho \equiv 1 - l_{hy}/l_t$.

Note that the length scale l_t as given by (5.3) depends both on the protrusion length l_{pr} and on the hydration length l_{hy}. For $l_{hy} \gg l_{pr}$, one has $l_t \approx l_{hy}$; *i.e.*, in the limit in which the hydration potential has a much longer range than the effective protrusion potential, the mean separation is solely determined by the balance between the applied pressure and the repulsive hydration forces.

5.1 Gaussian models

Let us introduce two additional dimensionless quantities for the soft wall interaction *via*

$$z_{hy} \equiv l_{hy}/l_{sc} \qquad \text{and} \qquad U_{hy} \equiv A_0 V_{hy}/T. \tag{5.5}$$

The above results for the pressure-dependence of ℓ and $\xi_\perp$ are confirmed by MC simulations of the discrete Gaussian model, as shown in Figures 8, 9.

As we have already shown in the preceding section, the probability distribution $\mathcal{P}(l)$ for the discrete Gaussian model with a hard wall interaction has no exponential tail. In the presence of the hydration interaction, this distribution is well fitted by the functional form

$$\mathcal{P}_{Gau}(l) \sim \exp\left[-\frac{(l-\ell)^2}{2\xi_\perp^2} - U_{hy} e^{-l/l_{hy}}\right], \tag{5.6}$$

where the influence of the direct hydration potential has been taken into account in the simplest possible manner. Note that the term that explicitely depends on the hydration potential in (5.6) is appreciable only for $l \lesssim l_{hy}$, *i.e.* close to the hard wall, while ℓ diverges in the limit of small P. Figure 10 shows some fits of this form. Obviously, the tails have pronounced Gaussian characteristics, rather than exponential tails, on *both* sides. On the side facing the wall, the fits are excellent, while they are slightly poorer on the other side.

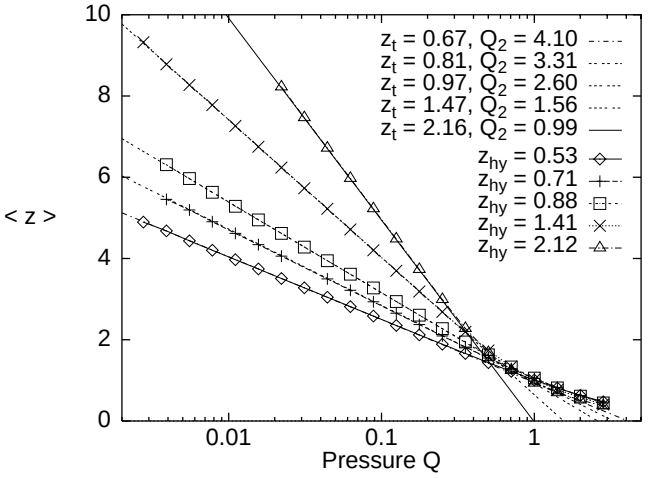

Fig. 8. Discrete Gaussian model: Mean distance $\langle z \rangle$ *versus* pressure Q for several hydration lengths z_{hy} for one surface fluctuating against a soft wall, with a linear dimension $L_\parallel = 64$ and potential strength $U_{hy} = 5.7$. The data are fitted by the functional form $z = z_t \ln(Q_2/Q)$.

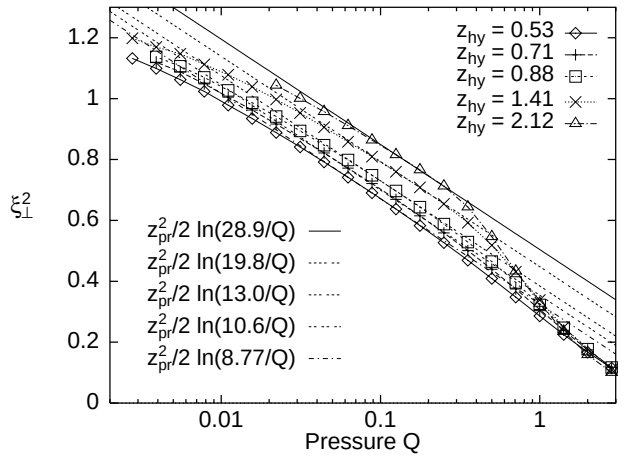

Fig. 9. Discrete Gaussian model: Roughness $\xi_\perp^2$ *versus* pressure Q from the same MC data as in Figure 8. For the fit, the value $z_{pr}^2/2 = 0.15$ has been used, corresponding to $z_{pr} \simeq 0.55$. Note the finite size effects for $Q \lesssim 0.02$.

An evaluation of the Gaussian distribution $\mathcal{P}_{Gau}(l)$ at the position $l = 0$ of the hard wall, leads to the contact probability

$$\mathcal{P}_{2b} \sim e^{-\ell^2/2\xi_\perp^2} \sim P^{(l_t/l_{pr})^2}, \tag{5.7}$$

in the limit of small pressure P, where the pressure dependence of $\xi_\perp$ and ℓ as given by (4.8) and (5.2), resp., has been used, ignoring confluent logarithmic terms.

Thus, the contact exponent ν_2 is found to be

$$\nu_2 = (l_t/l_{pr})^2, \tag{5.8}$$

where the length scale l_t is given by (5.3). Note that for $l_{hy} = l_{pr}/2$, which defines the border line between the protrusion and the hydration regime, one has $l_t = l_{pr}$ and

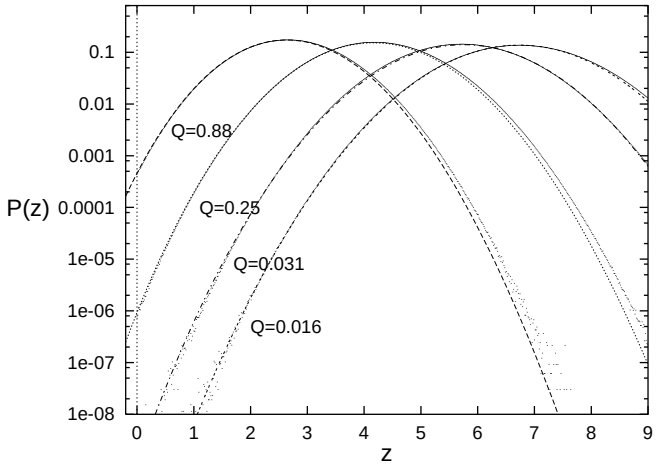

Fig. 10. Typical histograms for the Gaussian model with a soft wall. Sample size 64×64, $U_{hy} = 5.7$, $z_{hy} = 1.41$. The fitting curves have the functional form $\exp(-(z - \langle z \rangle)^2/2\xi_\perp^2 - U_{hy} e^{-z/z_{hy}})$. Note the absence of exponential tails.

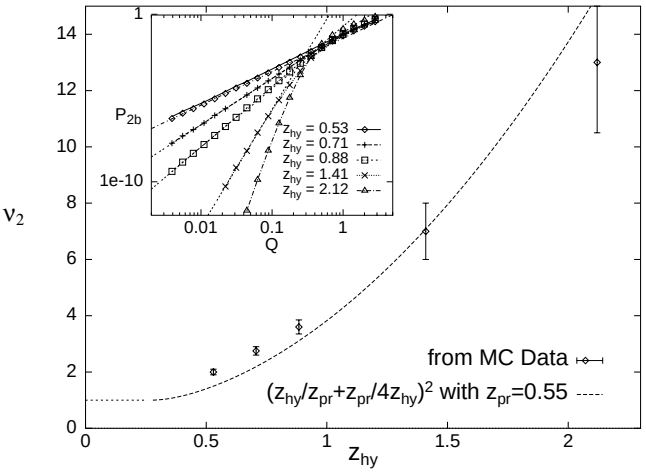

Fig. 11. Contact exponents ν_2 as a function of the hydration length z_{hy} for the discrete Gaussian model. In the inset, fits to MC data for the contact probability $\mathcal{P}_{2b}$ *versus* pressure Q are shown.

hence $\nu_2 = 1$ as in the protrusion regime. Therefore, the contact exponent ν_2 is a continuous function of l_{hy}.

The corresponding data from MC simulations of the discrete Gaussian model are shown in Figure 11. An inspection of this figure reveals considerable deviations from the predicted values as given by (5.8). These deviations can be explained in the following way.

First of all, the accessible regime of pressure values Q is quite restricted, covering only about one order of magnitude: For large $Q > 1$, we are deep in the mean field regime where the collective behavior is dominated by the external pressure. In the latter case, the molecules move almost independently and the probability distibution is $\sim Q \exp(-Qz)$. This implies that the contact probability scales linearly with Q, not depending on the details of the hydration force. For small $Q \lesssim 0.01$, on the other hand,

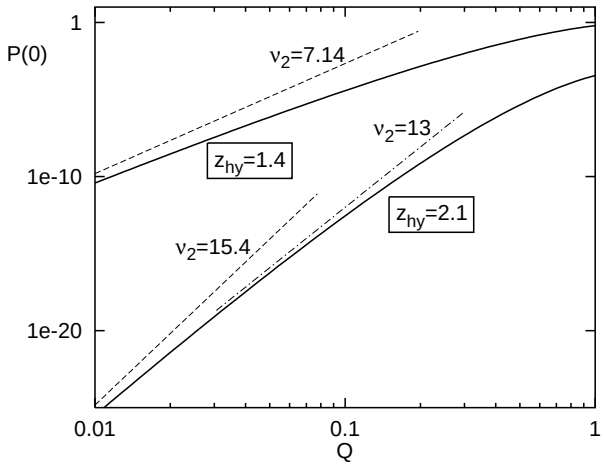

Fig. 12. Contact exponents for the discrete Gaussian model with soft wall interaction. The upper curve corresponds to $z_{hy} = 1.4$, the lower one to $z_{hy} = 2.1$. For a detailed discussion of this figure, see Section 5.1.

the finite size of the sample effects the interface roughness $\xi_\perp^2$, see Figure 9. This has a large effect on the histogram, making it 'narrower' than it would be for larger systems, while the mean distance ℓ is essentially unaffected by the finite size. This lowers the observed contact probability $\mathcal{P}_{2b} \sim \mathcal{P}(0)$. For this reason, we expect to extract a contact exponent from the data which is larger than the true asymptotic value. This behavior is expected for all values of z_{hy}, hence all data will tend to lie *above* the theoretical line.

Secondly, the asymptotic form for $\mathcal{P}_{2b}$ as given by (5.7) is difficult to extract from intermediate values of Q because of large corrections to the leading scaling behavior which arise as long as the pressure amplitudes Q_2 and $Q_{2\perp}$ take different values. Indeed, one has $\mathcal{P}_{2b} \sim \exp[-\ell^2/2\xi_\perp^2]$ with the asymptotic behavior

$$\frac{\ell^2}{2\xi_\perp^2} \approx \frac{l_t^2}{l_{pr}^2} \frac{\ln^2(Q_2/Q)}{\ln(Q_{2\perp}/Q)} = \frac{l_t^2}{l_{pr}^2} \left[\ln\left(\frac{Q_2^2}{Q_{2\perp} Q}\right) - \frac{\ln^2(Q_2/Q_{2\perp})}{\ln Q} + \mathcal{O}\left(\frac{1}{\ln^2 Q}\right) \right]. \tag{5.9}$$

The leading order correction vanishes only for $Q_2 = Q_{2\perp}$. Using the values for Q_2 and $Q_{2\perp}$ as measured in the MC simulations of the discrete Gaussian model, we find that these corrections affect our data both for $z_{hy} = 1.4$ and for $z_{hy} = 2.1$.

The measured contact exponents are however consistent with the actual values of $\exp[-\ell^2/2\xi_\perp^2]$ as determined from the measured values of ℓ and $\xi_\perp$. In order to show this, we have plotted $\exp(-l_t^2 \ln^2(Q_2/Q) \,/\, l_{pr}^2 \ln(Q_{2\perp}/Q))$, corresponding to the first equality in (5.9), as a function of Q, see Figure 12 (*full lines*). The values for Q_2 and $Q_{2\perp}$ were taken from the MC data. For comparison, we have included the expected asymptotic scaling function $\mathcal{P}_{2b} \sim Q^{z_t^2/z_{pr}^2}$, with the contact exponents $\nu_2 = z_t^2/z_{pr}^2 = 7.14$

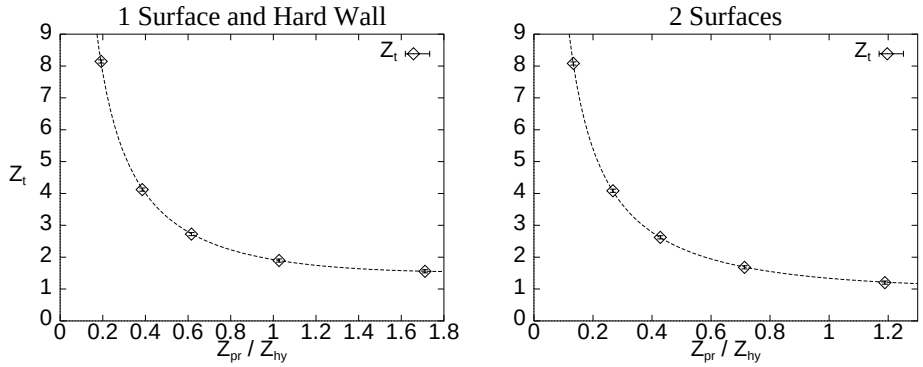

Fig. 13. Hydration regime in the SOS model: The length scale z_t is plotted *versus* z_{pr}/z_{hy}, for one and for two fluctuating surfaces. The broken curve corresponds to the prediction of functional renormalization as given by (5.3), $z_t = z_{pr}(z_{hy}/z_{pr} + z_{pr}/4z_{hy})$, with $z_{pr} = 1.54$ for one surface and $z_{pr} = 1.07$ for two surfaces.

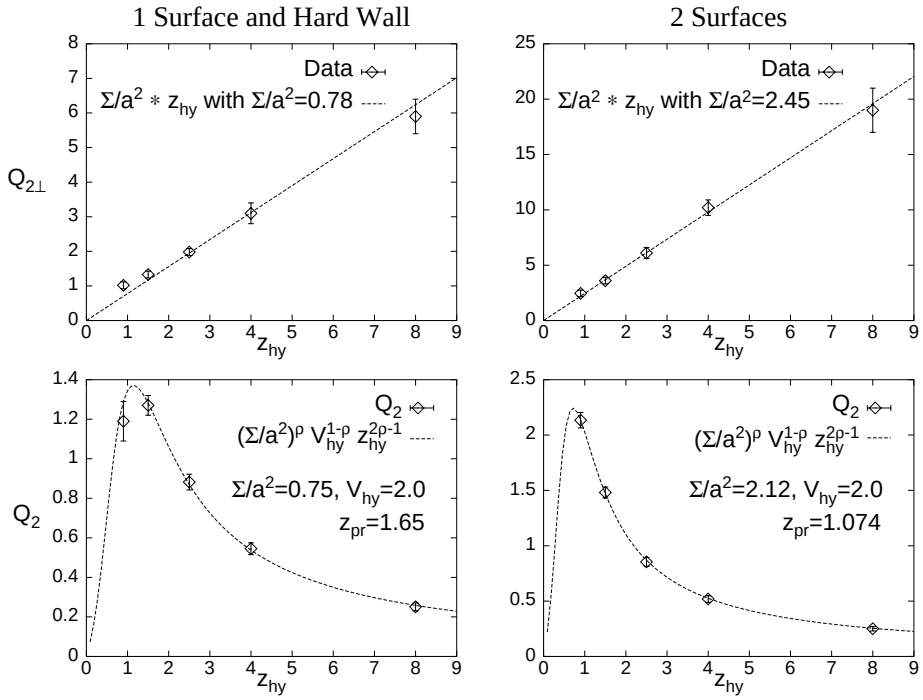

Fig. 14. The pressure amplitudes Q_2 and $Q_{2\perp}$ *versus* hydration length z_{hy}, for the SOS model of one and two fluctuating surfaces, respectively. For comparison, the formulae from equation (4.8) are plotted.

for $z_{hy} = 1.4$ and ν_2=15.4 for z_{hy}=2.1 (*dashed lines*). Finally, for the latter value $z_{hy} = 2.1$, the apparent scaling in the intermediate regime $0.03 \lesssim Q \lesssim 0.2$ with the exponent $\nu_2 = 13$ (as determined from MC data, see Fig. 11) is displayed (*dashed-dotted line*). Obviously, in the pressure regime that was accessible to MC simulations, this effective scaling exponent coincides well with the theoretical prediction. Note that this effect leads to data that are *lower* than the theoretical value for large values of z_{hy}.

Together, these two effects explain the deviations of the measured values for ν_2 from the theoretical prediction $\nu_2 = (l_t/l_{pr})^2$.

5.2 Solid–on–solid models

The SOS model with soft wall interactions has been expressed in terms of the dimensionless variables (5.5) and (4.16). Using this dimensionless form of the model, we have first studied the critical behavior of the mean separation ℓ and the roughness $\xi_\perp$. The corresponding MC data for $z_{hy} > z_{pr}/2$ are displayed in Figures 13 and 14. In these figures, we compare the critical behavior of (i) one fluctuating surface interacting with a hard wall and of (ii) two fluctuating surfaces. Inspection of these figures shows that both cases exhibit analogous critical behavior. We have also studied the critical behavior of ℓ and $\xi_\perp$ for smaller values of z_{hy}. All of these data are again consistent

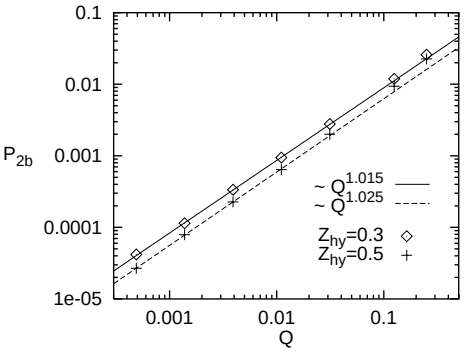

Fig. 15. Protrusion regime in the SOS model: Contact probability $\mathcal{P}_{2b}$ *versus* pressure Q with $z_{hy} < z_{pr}/2$. The data confirm the universal value $\nu_2 = 1$ for the contact exponent in this case.

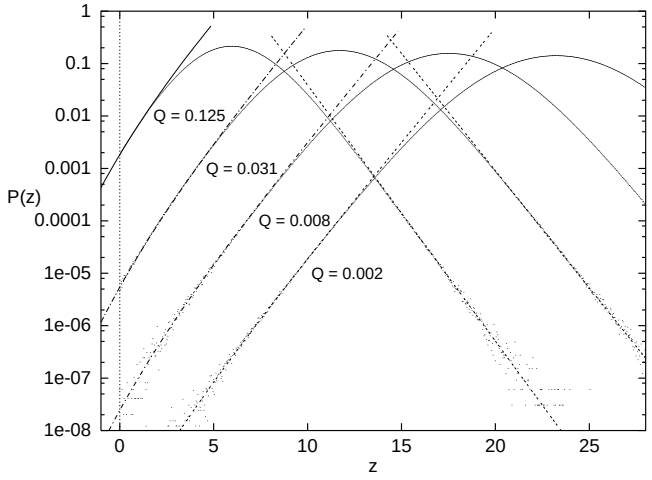

Fig. 16. Typical probability distributions $\mathcal{P}(z)$ for the SOS model with one fluctuating surface and a soft wall. The sample size was 64×64 sites, and the hydration interaction parameters were set to $U_{hy} = 2.0$ and $z_{hy} = 4.0$. The tails are well represented by a mean field like probability distribution $\mathcal{P}(z) \sim \exp(-|z - \langle z\rangle| - Qz - U_{hy}e^{-z/z_{hy}})$. Each tail has been fitted individually. In each fit, the only fit parameter was a constant factor. The difference to the histograms for the Gaussian model, where the exponential tails are absent, is obvious.

with two distinct scaling regimes: a hydration regime for $z_{hy} > z_{pr}/2$ and a protrusion regime for $z_{hy} < z_{pr}/2$.

Next, let us consider the contact probability $\mathcal{P}_{2b}$. In the protrusion regime, the mean separation between the membranes and their width are determined solely by the protrusion length l_{pr}, so the hydration interaction should not alter the pressure dependence of $\mathcal{P}_{2b}$. Thus, one expects again $\nu_2 = 1$. This is confirmed by numerical results that give the values $\nu_2 \simeq 1.015$ and 1.025 for $z_{hy} = 0.3$ and 0.5, respectively, which coincides with the expected value within the numerical precision, see Figure 15.

The situation changes when one enters the hydration regime with $z_{hy} > z_{pr}/2$. Now, the mean distance is proportional to l_t, while the roughness is still determined by l_{pr}. In the preceding chapter, we have found the value $\nu_2 = (l_t/l_{pr})^2$ for the hydration regime of the *Gaussian* model. However, we will now argue that, in the hydration regime of the *SOS* model, the contact probability $\mathcal{P}_{2b}$ is strongly affected by exponential tails of the probability distribution arising from molecular protrusions.

In the protrusion regime of the SOS model, the probability distribution $\mathcal{P}(l)$ has a pronounced exponential tail on the side of the interface which does not face the wall, while on the side facing the wall, it is essentially Gaussian shaped. This is the same behavior as observed in the case of pure hard wall interactions, as discussed in Section 4.2. Now, in the hydration regime of the SOS model, exponential tails are found on *both* sides of the histogram, as shown in Figure 16. This observation inspires a theoretical prediction for the contact exponent that yields a much better description of the data, based on the assumption that these tails are the result of isolated protrusions which can be considered as 'rare' events.

Thus, we should distinguish two different types of excitations: (i), *Collective* fluctuation modes that lead to a Gaussian shaped probability distribution and, consequently, to the contact exponent as given by (5.8); and (ii) *Isolated* protrusions of single molecules which are absent in the discrete Gaussian model.

Now, let us assume that the tails of the distribution $\mathcal{P}(l)$ and hence the contact probability $\mathcal{P}_{2b}$ is dominated by these rare protrusions. The simplest estimate for $\mathcal{P}_{2b}$ is now given by

$$\mathcal{P}_{2b}^{SOS} \sim \exp[-\ell/l_{sc}], \tag{5.10}$$

which describes the probability for a single protrusion mode to extend over the distance ℓ between the interface and the hard wall. With the scaling of ℓ as given by (5.2) and (5.3), we now find the contact exponent

$$\nu_2 = l_t/l_{sc} = (l_{hy}/l_{sc})[1 + (l_{pr}/2l_{hy})^2]. \tag{5.11}$$

Note that this value depends on the two ratios l_{hy}/l_{sc} and l_{hy}/l_{pr}.

Thus, the Gaussian fluctuations and the single protrusion modes lead to a different asymptotic behavior of the contact probability $\mathcal{P}_{2b}$. The true asymptotic behavior will be determined by those fluctuations which dominate $\mathcal{P}_{2b}$. This competition leads to another characteristic length scale l_{hy}^* which separates *two different scaling regimes within the hydration regime.*

Direct comparison of the contact probabilities $\mathcal{P}_{2b}$ as given by (5.7) and (5.10) leads to the characteristic length scale

$$l_{hy}^* = \frac{l_{pr}}{2}\left(z_{pr} + \sqrt{z_{pr}^2 - 1}\right). \tag{5.12}$$

With $z_{pr} = 1.54$, this implies $l_{hy}^* \simeq 2.71 \times l_{pr}/2 \simeq 2.09\, l_{sc}$.

The Gaussian fluctuations and the single protrusion modes dominate for $l_{hy} < l_{hy}^*$ and $l_{hy} > l_{hy}^*$, respectively. This leads to the contact exponent

$$\begin{aligned} \nu_2 &= (l_t/l_{pr})^2 \text{ for } \quad l_{pr}/2 \le l_{hy} \le l_{hy}^* \\ &= l_t/l_{sc} \quad \text{for } \quad l_{hy} \ge l_{hy}^*. \end{aligned} \tag{5.13}$$

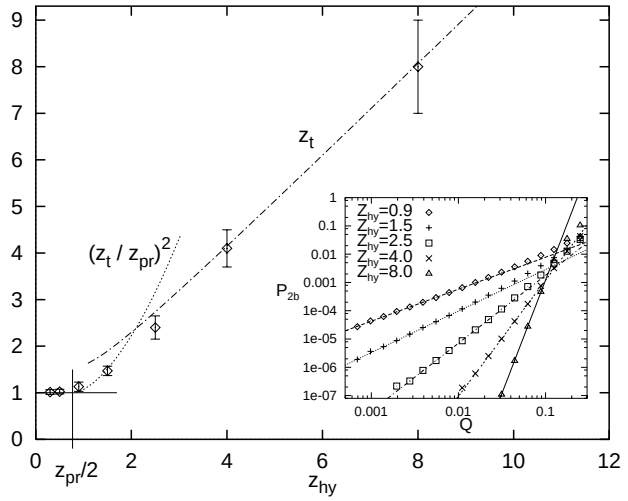

Fig. 17. MC data for a system with one flexible surface and a soft wall. The numerical data for the contact exponent ν_2 are compared with $\nu_2 = 1$ in the protrusion regime, and with the functions as given by (5.13) in the hydration regime: The dotted line corresponds to the prediction from Gaussian fluctuations, $\nu_2 = z_t^2/z_{pr}^2$, and the dashed-dotted line to $\nu_2 = z_t$. Here, we have used $z_{pr} = 1.54$. Note that these two curves cross at $z_{hy}^* = 2.09$. *Inset:* The MC data for $\mathcal{P}_{2b}$ are plotted *versus* the scaled pressure Q and fitted against $\mathcal{P}_{2b} \sim Q^{\nu_2}$. Apart from $z_{hy} = 8.0$, all data cover more than an order of magnitude in the pressure range and several orders of magnitude in $\mathcal{P}_{2b}$.

Table 1. The contact exponent ν_2 for the discrete Gaussian and the solid–on–solid models.

Contact exponent ν_2	$l_{hy} < \frac{l_{pr}}{2}$	$\frac{l_{pr}}{2} < l_{hy} < l_{hy}^*$	$l_{hy}^* < l_{hy}$
Discrete Gaussian model	1	$(\, l_t \,/\, l_{pr} \,)^2$	
Solid–on–solid model	1	$(l_t/l_{pr})^2$	l_t/l_{sc}

In Figure 17, MC data for the contact exponent in the SOS model are shown, together with the theoretical predictions (5.13). The different values of the contact exponent ν_2 are summarized in Table 1.

References

1. J. Rowlinson, B. Widom, *Molecular theory of capillarity* (Clarendon press, Oxford, 1982).
2. *Structure and dynamics of membranes*, Vol. 1 of *Handbook of biological physics*, edited by R. Lipowsky, E. Sackmann (Elsevier, Amsterdam, 1995).
3. G. Forgacs, R. Lipowsky, T. Nieuwenhuizen, in *Phase transitions and critical phenomena*, Vol. 14, edited by C. Domb, J. Lebowitz (Academic press, London, 1991), pp. 136–363.
4. S. Dietrich, in *Phase transitions and Critical Phenomena* Vol. 12, edited by C. Domb, J. Lebowitz (Academic Press, 1988).
5. M.E. Fisher, in *Statistical mechanics of membranes and surfaces*, edited by D. Nelson, T. Piran, S. Weinberg (World Scientific, 1989).
6. M. Schick, in *Liquids at Interfaces*, edited by J. Charvolin, J.F. Joanny, J. Zinn–Justin (North–Holland, 1990).
7. R. Lipowsky, M.E. Fisher, Phys. Rev. Lett. **57**, 2411 (1986); R. Lipowsky, M.E. Fisher, Phys. Rev. B **36**, 2126 (1987).
8. R. Lipowsky, S. Grotehans, Europhys. Lett. **23**, 599 (1993); and Biophys. Chem. **49**, 27 (1993).
9. R. Lipowsky, Z. Phys. B **97**, 193 (1995).
10. K. Binder, D.P. Landau, Phys. Rev. B **37**, 1745 (1988).
11. The interface in the 3–dimensional Ising model should undergo a roughening transition at a characteristic temperature $T = T_r$. Thus, one must in general distinguish a low–temperature regime with $T < T_r$ from a high–temperature regime with $T > T_r$. Here, we are only concerned with the latter regime.
12. G. Gompper, D. Kroll, R. Lipowsky, Phys. Rev. B **42**, 961 (1990).
13. R. Lipowsky, in *Surface X–ray and Neutron Scattering*, edited by H. Zabel, I. K. Robinson (Springer Verlag, Berlin 1992).
14. R. Rand, V. Parsegian, Biochim. Biophys. Acta **988**, 351 (1989).
15. S. Marcelja, N. Radic, Chem. Phys. Lett. **42**, 129 (1976).
16. E. Egberts, H. Berendsen, J. Chem. Phys. **89**, 3718 (1988).
17. R.W. Pastor, Curr. Opin. Struct. Biol. **4**, 486 (1994).
18. S. König *et al.*, J. Phys. II France **2**, 1589 (1992).
19. M. Wiener, S. White, Biophys. J. **61**, 434 (1992).
20. T. McIntosh, S. Simon, Biochemistry **32**, 8374 (1993).
21. J. Israelachvili, H. Wennerström, Langmuir **6**, 873 (1990).
22. F. Brochard, J.F. Lennon, J. Phys. France **36**, 1035 (1975).
23. W. Helfrich, W. Harbich, Chemica Scripta **25**, 32 (1984).
24. E. Evans, D. Needham, J. Phys. Chem. **91**, 4219 (1987).
25. E. Evans, W. Rawicz, Phys. Rev. Lett. **64**, 2094 (1990).
26. R. Netz, R. Lipowsky, Europhys. Lett. **29**, 345 (1995).
27. M. Lässig, R. Lipowsky, Phys. Rev. Lett. **70**, 1131 (1993).
28. M. Lässig, Phys. Rev. Lett. **73**, 561 (1994).
29. C. Hiergeist, M. Lässig, R. Lipowsky, Europhys. Lett. **28**, 103 (1994).
30. C. Hiergeist, R. Lipowsky, Physica A **244**, 164 (1997).
31. K.G. Wilson, Phys. Rev. B **4**, 3184 (1971).